scientific reports

OPEN

Wave energy converters as offshore wind farm guardians: a pathway to resilient ocean systems

Olivia Vitale[1]✉ & Maha N. Haji[2]

Maximizing the durability and reliability of offshore wind farms is essential for the clean energy transition. In this work, we demonstrate how wave energy converter (WEC) farms can shelter offshore wind farms from cyclic wave loading, resulting in significant reductions in wave-induced turbine fatigue damage. Using experimentally validated hydrodynamic models, we show that modeling WEC energy dissipation through fluid structure interactions rather than rated power provides an unbiased analysis of different architecture's sheltering capabilities. Through the system-level model, we observe that even small reductions in wave height propagate to the levelized cost of energy (LCOE) of the wind farm, resulting in a 4.94% decrease in LCOE with a 6% reduction in wave height. Additionally, WEC farms can benefit from this co-location by sharing siting costs, operation and maintenance teams, and mooring and transmission cables with the offshore wind farm. This work advances the design of integrated wind–wave systems, supporting resilient, cost-effective offshore renewables for global deployment.

Keywords Wave energy, Offshore wind, Wave sheltering

The power production potential for offshore wind has led to large current and projected growth in global installed capacity[1,2]. Despite its relevance to the modern grid, the intermittency of wind power results in power quality disturbance to the grid, harming electrical components[3]. The intermittency also increases the required storage capacity and reduces power reliability, pointing to a need for power smoothing[4]. Several studies have proposed co-locating wave energy converter (WEC) and wind farms for power extraction symbioses[5–11]. Kluger et al.[12] studied a combined WEC and offshore wind farm with 100 6 MW turbines and a variable number of 286 kW WECs. They found a 15% smoother power output when 50% of the turbines had a WEC attached to their platform compared to a standalone wind farm. Additionally, Astariz et al.[13] investigated the Alpha Ventus wind farm, composed of 12 5 MW turbines. They found an increase in allowable windows for maintenance due to the presence of an upstream WEC array containing between nine and 32 WaveCat[14] devices. This prior work is an initial motivator for the co-location of these offshore systems. However, as wave energy is less technologically mature than wind energy, additional benefits must be evaluated to further motivate this co-location.

Installing wind turbines offshore introduces significant additional fatigue stresses due to wave loading, reducing the turbine's lifetime[15,16]. For fixed-bottom offshore wind, wave-induced fatigue loads have caused monopile diameters to increase around 60%[17] or required developers to use jacket structures[18], creating a new trade-off between substructure lifetime and capital costs. These problems are exacerbated for floating offshore wind, where ocean waves also induce loads on mooring cables and floaters and cause oscillations of the turbines themselves[19,20]. Deploying a WEC farm upstream of an offshore wind farm can dampen incoming waves before they reach the downstream turbines, sheltering the wind farm.

Many studies have evaluated WEC sheltering for coastlines or offshore aquaculture farms[21–23], evaluating WEC sheltering with respect to number of WEC devices, distance between WECs, and WEC architecture type. However, results from these studies cannot be directly applied to offshore wind farms, as the fluid physics representing coastal regions is not representative of locations hosting offshore wind. Additionally, most WEC sheltering studies face serious limitations and inaccuracies due to simplifying assumptions in their WEC farm models.

Current wave sheltering studies simplify the WEC's dissipative properties, assuming the only energy removed from the waves is energy the device captures. Contardo et al.[24] used this power capture method to model their WEC's sheltering capabilities. They then completed two deployments of their physical WEC device, concluding

[1]Sibley School of Mechanical and Aerospace Engineering, Cornell University, Ithaca, NY 14850, USA. [2]Department of Mechanical Engineering, University of Michigan, Ann Arbor, MI 48109, USA. ✉email: ov35@cornell.edu

this method was poor at predicting actual wave sheltering. This is due to the method ignoring the energy that WECs scatter and dissipate through fluid-structure interactions, separate from the energy they capture. A few studies have attempted wave sheltering characterization methods that account for the fluid-structure interactions[25–27]. However, they are all conducted in coastal regions and can not be directly applied for offshore wind. Crucially, these studies, and all WEC sheltering studies to date, neglect hydrodynamic interactions between WEC devices in a farm. WECs disturb the nearby wave field and, when configured in arrays, disturb the motion of the nearby devices[28,29]. These interactions are relevant for determining device motion and power extraction performance[28]; however, the impact of these interactions on the larger ocean environment has not been studied. Zou et al.[30] attempted to capture WEC array wake effects by accounting for power extracted throughout the array, but still neglected hydrodynamic interactions.

Despite numerous WEC sheltering studies (synthesized in the Appendix), existing work treats wave sheltering, fluid-structure interactions, and array hydrodynamics as separate problems. Additionally, most studies focus on coastal regions, so structural fatigue loading and economic implications are absent from their analyses. A few models have investigated WEC sheltering explicitly for offshore wind[31,32], but only employ the power capture method. A unified framework connecting these layers has not been implemented. Existing offshore wind-wave co-location studies model WEC sheltering using power-capture-only dissipation and evaluate fatigue reductions without accounting for multi-body hydrodynamic interactions. As a result, the role of scattering, radiation, and array coupling in determining downstream wave attenuation remains unresolved, and architectural comparisons between WECs may be biased.

Here, we address this gap by experimentally validating a coupled hydrodynamic framework that captures full fluid–structure and hydrodynamic interactions within WEC arrays and propagates their effects to offshore wind turbine fatigue and economic performance. Wave height is measured upstream and downstream of the devices to quantify transmission and reflection coefficients[33,34], which are then integrated into a near-field boundary element method (BEM) and far-field spectral model. The resulting wave height reduction is directly translated into wave-induced monopile fatigue damage and lifetime-cost tradeoffs under representative offshore conditions. In summary, the presented framework:

1. evaluates multiple WEC architectures using full fluid-structure interaction rather than rated power assumptions,
2. explicitly accounts for multi-body hydrodynamic interactions in array configurations,
3. quantifies the propagation of wave height reduction to wave-induced fatigue damage for representative offshore wind conditions, and
4. demonstrates the resulting lifetime-cost tradeoffs through an illustrative LCOE sensitivity analysis.

WEC devices

The two WEC architectures evaluated in this study are shown at full ocean-scale in Fig. 1. The first architecture is called an oscillating surge WEC (OSWEC), a flap which extracts power from the waves through oscillatory pitching motion. The second architecture is a heaving point absorber (PA), a cylindrical buoy extracting power from the ocean waves by following their up-and-down (heave) motion. These architectures correspond to classes of devices under commercial development, such as the Carnegie Clean Energy CETO device[35], the heaving CorPower device[36], and the WaveRoller OSWEC[37]. Our prototypes are research-scale geometries inspired by reference models from Sandia National Labs and the National Lab of the Rockies[38], but they are not exact replicas. Extensive details on the design and build of the prototypes in this study can be found in Vitale et al.[39]. The OSWEC's width orthogonal to the incident wave direction is 18 m, while the PA's is 14.6 m. These dimensions were chosen based on the physical, tank-scale prototypes, built at the 1:50 Froude scale. The natural oscillation period of the OSWEC is 21 s, while the PA's is 5.09 s at full-scale. Both architecture prototypes

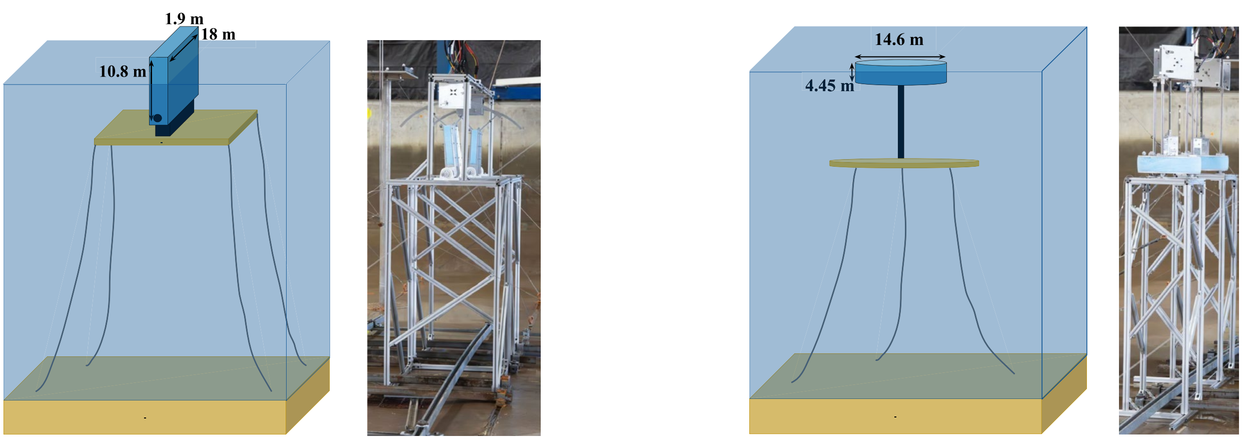

(a) OSWEC (b) PA

Fig. 1. Depiction of the two common WEC architectures evaluated in this study. Relevant dimensions are provided in the drawing, and images of the physical prototypes are shown next to the drawing for context.

employed a mechanical rack-and-pinion power take-off (PTO) mechanism to drive a motor-generator, shown in the Appendix. The PTO is how the devices extract energy from the waves, proportional to the damping present in the PTO. Each device's mechanical power extraction at full ocean-scale was estimated based on the tank-scale experiments. Each WEC's power extraction was different based on its position in the array. This is due to the hydrodynamic interactions between devices, where some devices experience motion amplification and others see decreased performance. The OSWECs predicted power extraction at the peak spectral period (11 s) is between 145 and 932 W based on position in the array. For the PAs, the mechanical power extraction is between 86.2 and 523 W.

Results

Wave sheltering performance

The wave sheltering performance was analyzed under oceanic conditions corresponding to the South Fork Wind Farm off the coast of Rhode Island. The farm consists of 12 turbines with a total farm rated power of 132 MW. A Pierson-Moskowitz spectra with a wind speed of 5.05 m/s at 19.5 m above sea level was used to represent the location. This corresponds to a significant wave height (H_s) of 2.19 m, a peak period (T_p) of 11 s, and an average period (T_a) of 5 s. The WECs were modeled in a 4-body farm to determine their individual sheltering capacities, including hydrodynamic interactions between devices. This 4-body unit was then repeated to produce a 20-body farm for the two different WEC architectures. These repeated units were placed 200 m apart, a large enough distance that interactions can be ignored[28]. The wave height disturbance in lee of these farms over 4000 m is shown in Fig. 2. The disturbance is the ratio of the wave height when the array is present to the wave height without any obstructions, where a value less than one indicates a reduction in wave height.

Since the OSWECs' rated mechanical power extraction is nearly double that of the PAs, traditional power-capture modeling methods would predict the OSWEC to significantly outperform the PA in terms of wave sheltering. However, the PAs demonstrate only 0.4% less wave height reduction with around a 50 m wider

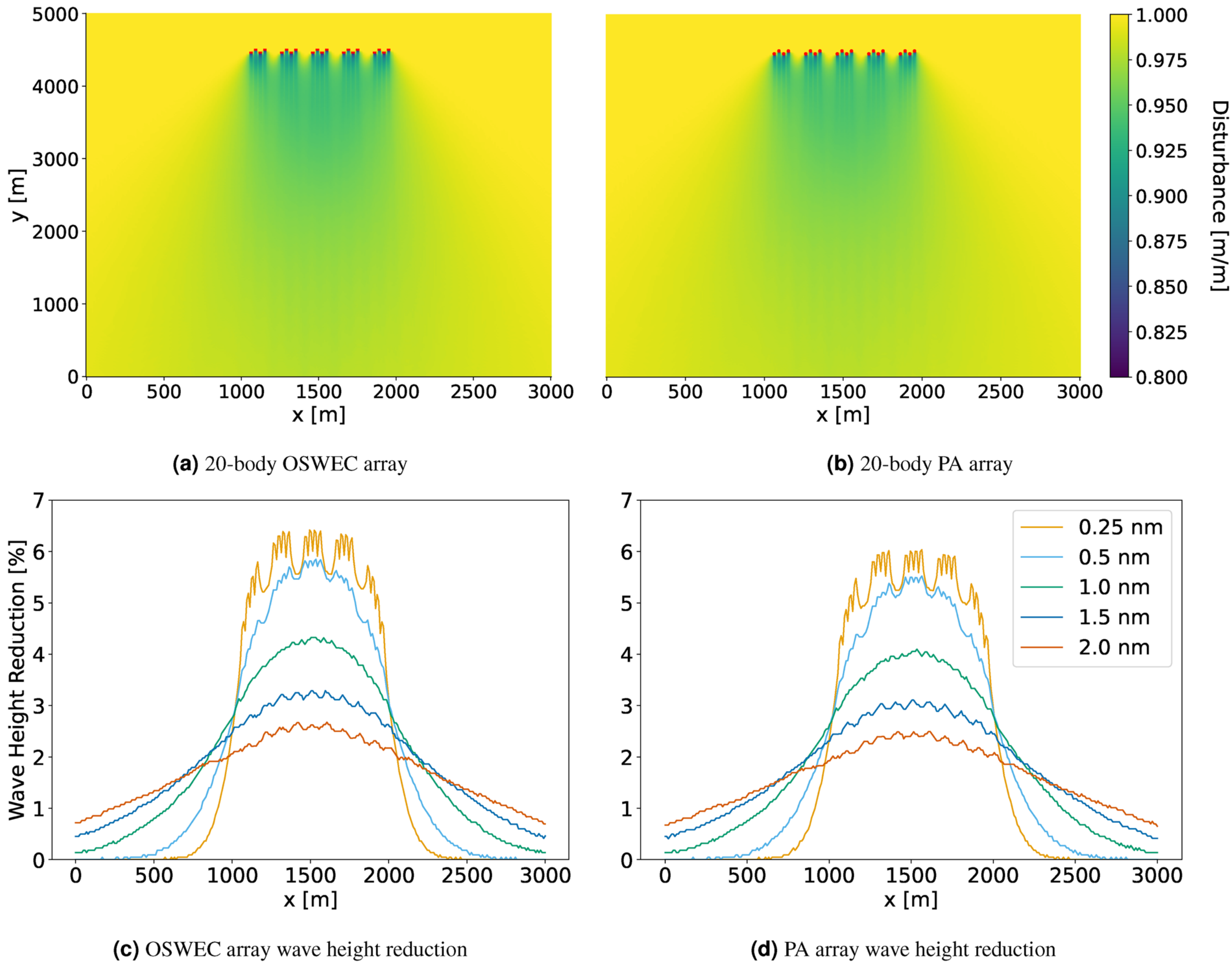

Fig. 2. Wave height computed by the spectral balance solver in lee of a 20-body (**a**) OSWEC array and (**b**) PA WEC array. Red markers indicate WEC devices. (**c**) and (**d**) show the percent wave height reduction at five y-distances from the arrays.

wake compared to the OSWECs. When accounting for array and fluid-structure interactions, the sheltering effect produced by the two architectures is nearly identical. This highlights the importance of including these interactions in a sheltering model, as the dissipative properties of these floating devices includes more than their isolated rated power capture. This has both policy and design implications for co-locating wind-wave systems. Currently, it is common practice to deploy an energy farm based on its total power production capacity. However, this does not accurately predict the WEC farm's sheltering capabilities. If sheltering is a primary driver of co-location, then cost, manufacturability, and co-location logistics should take precedent over power rating of the WEC device.

Wave-induced fatigue damage reduction

Even small reductions in wave height provide large reductions in wave-induced fatigue damage over the lifetime of an offshore wind turbine. For inertia-dominated loading, stress ranges scale approximately with wave height, and fatigue life scales nonlinearly with stress via the S–N slope (m=5), so modest wave height reductions can yield amplified reductions in wave-induced fatigue damage. It should be noted that the purpose of this modeling is to identify the sensitivity of wave-induced damage to upstream hydrodynamic modification, rather than to replace full aero-hydro-servo-elastic simulations, which are required to estimate the full fatigue damage on the monopiles.

The 20-body farms achieved up to 6.42% wave height reduction at 0.25 nm (463 m) in lee of the devices and between 1.0–2.68% reduction at 2 nm (3,704 m). This corresponds to between 5.03–28.85% reduction in wave-induced fatigue damage on the turbine monopiles. Three potential co-location configurations of the South Fork wind farm and a WEC farm are shown in Fig. 3. Placing the farms at 0.25 nm apart results in the largest wave-induced fatigue damage reduction, but a reduced breadth of sheltering. This can be balanced by either adding more WECs to the farm to increase the sheltering width or by moving the turbines further downstream. Due to the South Fork wind farm configuration, the nearest turbine does not always experience the greatest sheltering. This points to a co-location optimization problem, designing the wind-wave farm to maximize the sheltering effect. The achievable reduction in wave-induced fatigue could enable downsized monopiles to be feasible, reducing waste as well as the total cost of energy. The relationship between lifetime extension, monopile size reduction, and effect on cost is explored in the following section.

Cost and deployment

There is a tradeoff between the size of the turbine monopiles and the cycles to failure due to wave loading, and this relationship is shown in Fig. 4afor five extra-large monopile sizes. It is observed that for this farm location, there is about half an order of magnitude difference in cycles of failure due to wave loading between the 11 m and 7 m extra large monopile sizes. The wave loads are only a portion of the total loads on the offshore wind turbines, but the fatigue damage the turbines accrue due to wave loading can be significant based on monopile size[40]. The fatigue damage (D) communicates the portion of the total fatigue lifetime of the structure that has been used due to a particular load or all the combined load cases. To clarify, as D approaches 1, the structure approaches the end of its life. The years of turbine life that are used due to only the wave loads is shown in Fig. 4bfor the same cases of monopile size and wave height reduction previously mentioned. For the largest monopile diameter, like the ones

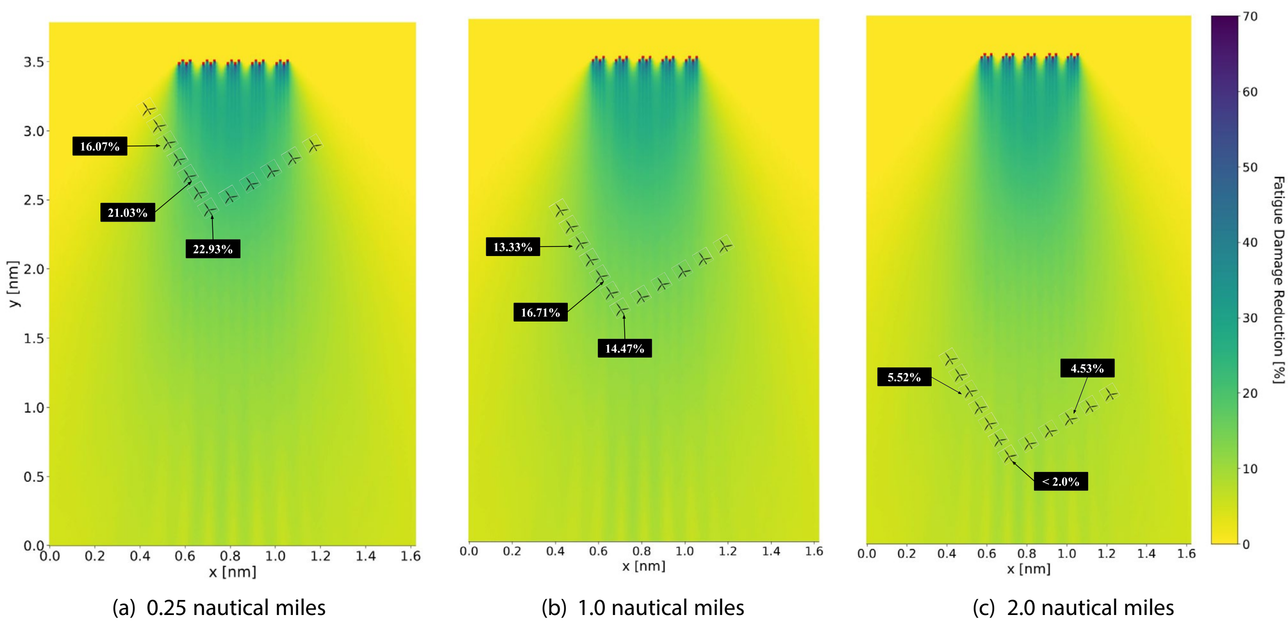

Fig. 3. Depiction of wave-induced fatigue damage reduction at representative turbines in the South Fork wind farm due to the WEC farm. (**a**) shows results for when the start of the wind farm is 0.25 nm away from the WEC farm, (**b**) shows a distance of 1.0 nm, and (**c**) shows a distance of 2.0 nm.

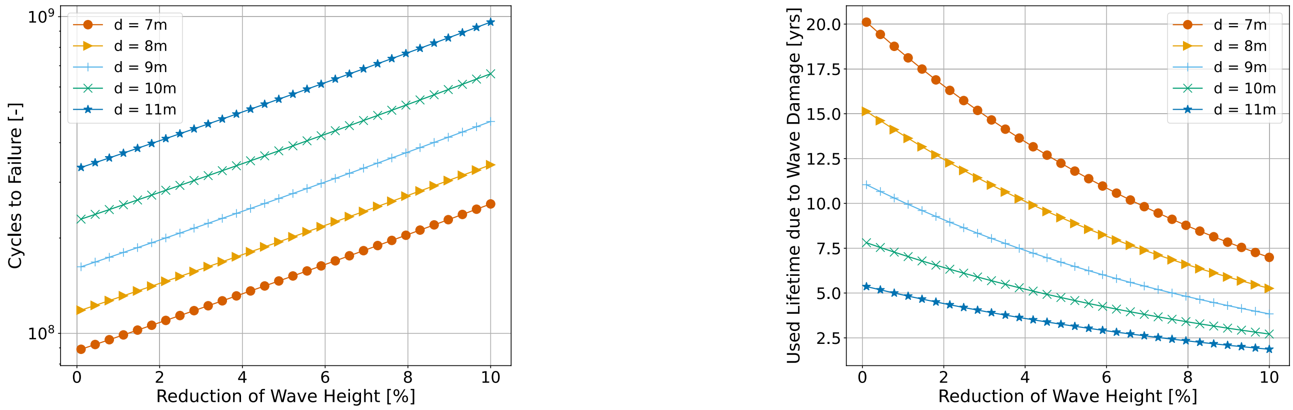

(a) (b)

Fig. 4. (**a**) Cycles of wave loading on the monopile to failure (N_f) and (**b**) Amount of lifetime (in years) that is used due to wave-induced fatigue damage with respect to reduction in wave height for five extra large monopile sizes.

used at South Fork, the fatigue damage due to wave loads only consumes five years of the turbine's total fatigue life (assumed to be the nominal 25 years). However, even a small reduction in wave height, around 6%, can cut that lifetime usage in half to 2.5 years. For thinner monopiles, fatigue damage due to wave loading is far more impactful to the turbine lifetime, claiming up to 20 years of fatigue life in the case with 0% wave height reduction. However, the thinner monopiles also see the greatest benefit from wave height reduction, with a 6% reduction in wave height reducing the lifetime usage due to wave loading down to 10 years for the smallest monopile size.

With this result, we can explore several potential design configurations. For example, if the acceptable number of years of fatigue life used due to wave loading is less than ten years, then 10 and 11 m monopile diameters are acceptable without any wave height reduction. However, 7, 8, and 9 m monopile diameters are acceptable if 6.90%, 4.10%, and 1.65% wave height reduction is achieved, respectively. With the bottom line typically being cost, the sensitivity of the cost of energy to monopile costs and lifetime must be evaluated to determine favorable configurations.

The levelized cost of energy (*LCOE*) then be considered for the wind farm. The tower and substructure (monopile, in this case) materials and installation account for 11.96% of the total system capital costs (*CAPEX*). Reducing the monopile size can propagate the reductions in these capital costs. However, the *LCOE* of the system is highly sensitive to turbine lifetime[41]. To evaluate this tradeoff, we present two scenarios where the wave height is reduced by 6%: 1) the monopile size remains the same and the lifetime increases by 2.5 years from nominal and 2) the monopile size is reduced by 27% but the lifetime decreases by 2.5 years from nominal. The nominal case is the 11 m diameter monopile with a turbine lifetime of 25 years and 0% wave height reduction. This assumes that in the nominal case, 5 years of the total turbine fatigue life are used up by wave loading, and the rest of the fatigue life is attributed to other loads (such as aerodynamic loads). Therefore, we assume that by reducing the fatigue life years consumed by wave loading, the lifetime of the turbine will increase by the same amount.

For case 1, where *CAPEX* is kept constant but lifetime increases by 2.5 years, a 4.94% decrease in *LCOE* from nominal is observed for the wind farm. For case 2, the material and installation costs of the tower and substructure were reduced by 27%, assuming a linear scale of these costs with turbine size. However, with the 2.5 year decrease in lifetime, the *LCOE* increased by around 1.99% from nominal.

Discussion

Hydrodynamic interactions were found to be relevant in determining device dynamics. Accounting for them gives a more accurate representation of expected device performance in the near- and far-field. Additionally, including fluid-structure interactions in the model exposes the bias present in traditional power-capture modeling methods for wave sheltering. Though the OSWECs are rated for a much higher power extraction level, they do not significantly outperform the PAs when sheltering waves due to the importance of fluid-structure interactions. This suggests a potential tradeoff for hybrid wind-wave farm developers. The larger OSWECs may be more suitable for power production in the hybrid farm due to their higher rated power, but the smaller PAs may provide the same amount of wave protection at a potentially lower cost and simpler implementation.

Sheltering is greatest nearest to the array. This is an intuitive result, but the wave height reduction at larger distances should not be ignored. Even small reductions in wave height can significantly reduce wave-induced fatigue damage over an offshore wind turbine's lifetime, seeing a 10% reduction in wave-induced damage with only a 2% reduction in wave height. It should be noted that a simplified model was employed to represent only the fatigue loads due to incident waves, and aerodynamic loads and their couplings with wave loads are not included. Still, this wave-induced fatigue reduction can improve turbine lifetimes, or alternatively allow for smaller monopile diameter requirements, depending on a developer's goals and restrictions. However, this is not distributed evenly at each monopile in the wind farm. To achieve maximum wave-induced fatigue reduction, a wind-wave farm should be designed concurrently, with the turbine and WEC placement in careful consideration.

The wave-induced fatigue damage reduction can propagate to the *LCOE* through a combination of lifetime extension and material reduction. Typically, the reduced monopile sizes will see a reduced fatigue life and an overall increase in *LCOE*. However, this may be preferred for smaller farm sites or for developers looking to reduce material usage for sustainability purposes. Additionally, small reductions in wave height can propagate to significant extensions in lifetime for the larger monopile sizes. This is especially relevant for the cost of the system, as the *LCOE* estimates are very sensitive to the lifetime of the turbine[41]. As presented above, at the 11 m monopile size, the *LCOE* can decrease by 4.94% with only a 6% reduction in wave height at each turbine. However, as stated above, a co-located wind-wave farm needs to be carefully designed to maximize the wave height reduction for the largest number of turbines.

The co-location of offshore wind and WEC farms presents a unique synergistic opportunity. In addition to their pre-established ability to provide power smoothing for the intermittent wind resource and increasing operation and maintenance windows, they offer a lifetime extension for offshore wind. This becomes increasingly relevant as wind moves further offshore, requiring protection from stronger waves. This coupling is also beneficial for the budding wave energy industry. Co-location offers the opportunity to share siting costs, mooring and transmission lines, and combine operation and maintenance teams. The results of this study indicate that co-located wind-wave farms present a promising pathway for the simultaneous achievement of wave-induced fatigue load reduction and increased renewable energy generation. This synergy facilitates not only maintenance and cost savings, but positions offshore farms as adaptable, resilient energy hubs central to future distributed ocean power systems.

Methods

This study required identification of the following key metrics: each device's dynamic response (response amplitude operator, *RAO*), the transmission (K_t) and reflection (K_r) coefficients, the far-field wave height reduction, and the wind turbine wave-induced fatigue damage. To quantify these metrics, an integrated model consisting of a near-field hydrodynamics solver and far-field wave propagation solver is required. The near-field solver computes the hydrodynamic properties of the WEC devices and the local disruption of the wave field. The *RAO*, K_t, and K_r are found through this solver. This hydrodynamic model was validated through an experimental campaign, with the open-source dataset and post-processing scripts available at the Marine and Hydrokinetic Data Repository. This experimental validation bolsters the fidelity of the model, adding confidence to the results. The far-field solver computes the wave propagation over several thousand kilometers due to the presence of the array. It relies on K_t and K_r to define the energy reduction due to the array. The far-field wave height reduction is found through this solver. A visual depiction of how these solvers interact is shown in Fig. 5a. The wind turbine wave-induced fatigue damage is found through Morrison wave force loading and the Palmgren-Miner rule. All software used to develop this work is available open-source, and the code used to generate the results can be found at the SEA Lab Github Repository. Further details on the model are provided in the following subsections.

Hydrodynamic modeling

WECs are modeled as second-order systems. They have hydrostatic parameters that are inherent to the device geometry and material properties, which are the mass/inertia matrix (M_{ij} [kg and kg-m^2]) and hydrostatic stiffness due to buoyancy (K_{ij}, [kg/s^2 and kg-m^2/s^2]). Additionally, there is a radiation force term to account for the reactive force from the fluid on the buoy due to the buoy's acceleration through the fluid. This term is broken down into the added mass matrix (A_{ij} [kg and kg-m^2]) and radiation damping (B_{ij} [kg/s and kg-m^2/s]) due to the device's oscillations. These are the hydrodynamic coefficients computed by the numerical solver, and are the matrices which eventually can be used to represent array hydrodynamic interactions. The hydrostatic and hydrodynamic coefficient matrices are used to compute $\hat{X}_i$ [m], the complex body motion, shown as

$$\frac{\hat{X}_i}{A} = \frac{\hat{F}_{ex,i}}{-\omega^2(M_{ij} + A_{ij}) - j\omega B_{tot} + K_{ij}} \tag{1}$$

for an isolated device, where *A* is the wave amplitude [m], ω is the wave frequency [rad/s], and $\hat{F}_{ex}$ is the wave exciting force on the body [N and N-m]. The "*i*" and "*j*" indices represent degrees of freedom of the body, ranging from 1 to 6. B_{tot} represents the total damping in the system, including B_{ij} and damping from the power take-off (B_{PTO}) based on Falnes' optimum control[42], expressed as

$$B_{PTO} = diag\left(\sqrt{B_{ij}^2 + \left(\omega(M_{ij} + A_{ij}) - \frac{K_{ij}}{\omega}\right)^2}\right) \tag{2}$$

These equations are for an isolated WEC floating body. However, in an array, the device's $\hat{X}_i$ equations are coupled, as their dynamic response depends on one another. To account for this in the model, each WEC device is allowed to oscillate in the single degree of freedom in which it extracts power. Then, the subscripts "*i*" and "*j*" in Eq. 1 can be used to denote the WEC device number rather than degree of freedom. For example, A_{12} is now the added mass in device 1's system due to device 2's oscillations. Accounting for all these couplings between devices is how the hydrodynamic interaction matrix is built and the coupled $\hat{X}_i$ of each device is determined. The response amplitude operator (*RAO*) is equivalent to the magnitude of the ratio between complex device motion and incident wave amplitude, shown by

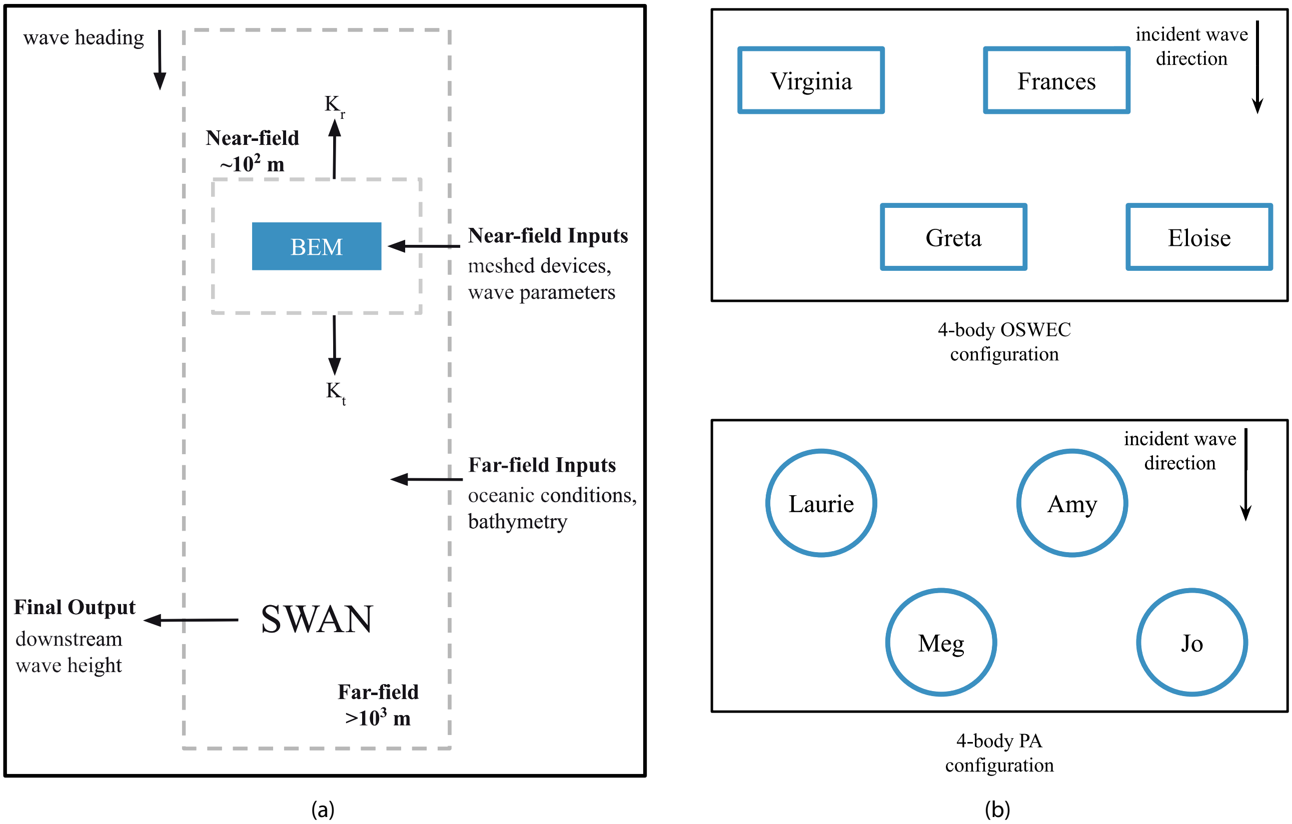

Fig. 5. (**a**) Graphical representation of hydrodynamic (near-field) BEM model interacting with the far-field spectral action model. (**b**) Four-body array configurations for oscillating surge WECs (top) and heaving point absorbers (bottom) that are meshed in the BEM solver.

$$RAO_i = \left|\frac{\hat{X}_i}{A}\right| \tag{3}$$

and the mechanical power (P_{mech} [W]) is computed as[42]

$$P_{mech} = \frac{1}{2}B_{PTO}|i\omega\hat{X}_i|^2 \tag{4}$$

This study utilizes an open-source boundary element method (BEM) solver called Capytaine[43] to compute these hydrodynamic coefficient matrices. This method employs frequency domain linear potential flow theory to solve the wave diffraction and radiation problems, assuming irrotational, incompressible, and inviscid flow. The linear potential flow problem is formulated using the Laplace equation ($\nabla^2\phi = 0$) for mass conservation where ϕ is the velocity potential defined as $u = \nabla\phi$. The solution is found through the frequency domain ($\phi = \mathbb{R}e\{\Phi e^{i\omega t}\}$). To solve this partial differential equation, we employ the following boundary conditions:

- the linearized free surface continuity equation: $\frac{\partial\hat{\Phi}}{\partial z} - \frac{\omega^2}{g}\hat{\Phi} = 0$ on $z = 0$,
- the zero-flux at sea bottom condition: $\frac{\partial\hat{\Phi}}{\partial z} = 0$ at $z = -h$, and
- given a velocity v on the body surface Γ: $\nabla\hat{\Phi} \cdot \mathrm{n} = \mathrm{v} \cdot \mathrm{n}$ on Γ,

and forces on the body are computed through the integration of the resulting pressure field. Details on the numerical implementation of this solver are available in the Capytaine theory manual[43]. Neglecting viscous friction is a significant shortcoming of these models and is addressed further in the Experimental Validation section.

The BEM solver is also used to compute the near-field wave elevation [m]. The wave field is the superposition of the incident wave elevation ($\hat{\eta}_{in}$), the diffracted wave elevation ($\hat{\eta}_{diff}$), and the radiated wave elevation ($\hat{\eta}_{rad,i}$), shown as

$$\hat{\eta} = \hat{\eta}_{in} + \hat{\eta}_{diff} + \sum_i \hat{\eta}_{rad,i}RAO_i \tag{5}$$

The radiated wave elevation produced from every relevant degree of freedom must be included in this superposition. Additionally, the radiated waves must be multiplied by the device's *RAO* to accurately represent their true magnitude. These computations are completed for individual frequencies (regular waves). However, the true ocean environment hosts multiple frequencies at once (irregular waves), with each wave frequency corresponding to a spectral density value. We represent this using a wave spectrum, and more details are provided in the Sheltering Characterization section. Details on the numerical convergence of the device meshes and the free surface mesh are provided in the Appendix, Section B.

Figure 5bdepicts the two WEC array configurations analyzed in this report, one consisting of four PAs and the other of four OSWECs. These configurations were determined from a brute force Monte Carlo Method optimization for fifteen different configurations over twelve sets of oceanic conditions. The configurations resembled common layouts found in literature as well as promising layouts from a previous optimization study[44], ranging from 3- to 5-body arrays. In the optimization, the x- and y-distance between devices was variable to determine the distance which maximized constructive hydrodynamic interactions for each of the fifteen possible configurations. This distance was numerically determined to be as close together as possible while avoiding device collision. The hydrodynamic interaction benefits were evaluated by the total expected mechanical power production of the farm, computed using Eq. 4. This, or electrical power production, is the current standard for evaluating WEC array performance. Therefore, the standard was followed to evaluate whether optimizing power production also optimizes wave sheltering.

The number of devices in the array was capped at five to maintain computational efficiency in the BEM model, as the computational complexity scales cubically with the number of evaluated panels[45]. An array consisting of four devices was eventually chosen due to the promising hydrodynamic interactions observed numerically and the feasibility of the physical prototype build timeline. The WEC array location relative to the offshore wind farm was not optimized, and was chosen to be upstream of the wind farm with respect to the dominant incident wave direction. Since waves are omnidirectional, a WEC-wind farm should be designed concurrently to increase the sheltering the turbines experience based on the most dominant wave directions. However, this is out of scope for the present study, as we evaluate an existing offshore wind farm design.

The devices were also tested in isolation to quantify to what extent array interactions affected hydrodynamic performance. The array interactions were experimentally found to significantly alter each individual WEC's response to incident wave conditions. These results are presented for the 1:50 scale WEC prototypes, corresponding to the scaled wave frequencies, ranging from around 4.5 to 6.5 rad/s (around 1.39 to 1.00 s periods). This tank-scale experimental data was used to tune the BEM model. The BEM model at full ocean-scale ultimately produced the data in the presented analysis.

Figures 6band 6ashows the experimentally measured *RAOs* of the isolated OSWEC and PA devices, respectively, demonstrating the hydrodynamic response without the presence of array interactions. When the devices are placed in the 4-body array configuration, their hydrodynamic response to the incident wave changes compared to the isolated response, shown in Figs. 6cand 6d. The isolated PA device hydrodynamic response resembles a classic second-order system, with a peak response at ω = 5.03 rad/s. However, once several PA devices are operating concurrently in an array (Fig. 6d), a second peak is identified in the response curves at ω = 4.72 rad/s. Additionally, the bandwidth of the response of each PA in different locations in the array varied widely. A similar result is observed for the OSWECs, with a significant drop in *RAO* between ω = 4.72 and 5.03 rad/s when placed in an array compared to when the OSWEC operates in isolation.

This result illuminates the significant impact of array interactions on individual device hydrodynamic response to incident waves. When the devices are modeled in isolation but applied in an array, this crucial impact on device response is neglected. This leads to a misrepresentation of array performance, both in power production and sheltering.

Sheltering characterization

To determine each device's effect on the wave field, the transmission (K_t) and reflection (K_r) coefficients were defined. The coefficients represent the amount of wave energy that transmits past the device and the energy that is reflected back upstream by the device, respectively. These coefficients are defined as

$$K_t = \frac{|\hat{\eta}_{down}|}{|\hat{\eta}_{in}|} \tag{6}$$

and

$$K_r = \frac{|\hat{\eta}_{up}| - |\hat{\eta}_{in}|}{|\hat{\eta}_{in}|} \tag{7}$$

where "up" and "down" denote the total wave elevation upstream and downstream of the device, respectively. A visual representation of these wave elevations with respect to the device is shown in Fig. 7. These coefficients were found numerically in the BEM solver. The average value of the wave elevation over one wavelength in front of and in lee of the device were used to determine the coefficients. The numerically computed free surface was validated with experimental data, with more details in the Experimental Validation section.

These coefficients were computed under regular wave inputs (i.e., one wave frequency at a time). To account for the spectral behavior (multiple wave frequencies at once) of the real ocean environment, the expected value of the coefficients in the wave spectra at the South Fork Wind Farm location was computed for each device. The Pierson-Moskowitz spectrum ($S(\omega)$ $[\frac{m^2}{rad/s}]$) was represented as[46]

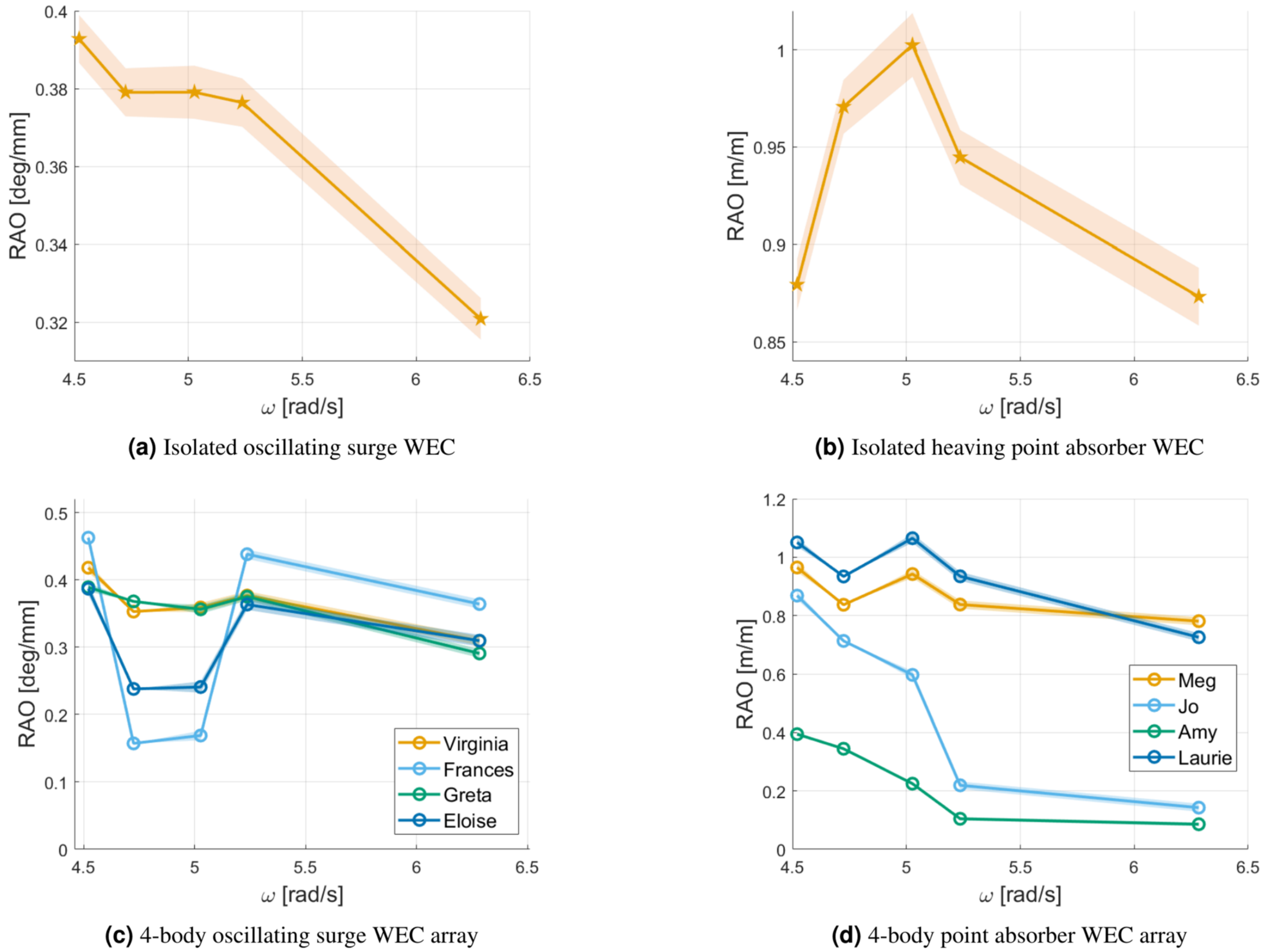

Fig. 6. Device response amplitude operators for (**a**) an isolated heaving point absorber WEC, (**b**) an isolated oscillating surge WEC, (**c**) a 4-body point absorber WEC array, (**d**) a 4-body oscillating surge WEC array. The names in the legends correspond to physical devices from experimentation, shown in Fig. 5b. Shading around the lines indicates the 95% confidence interval bounds on the data.

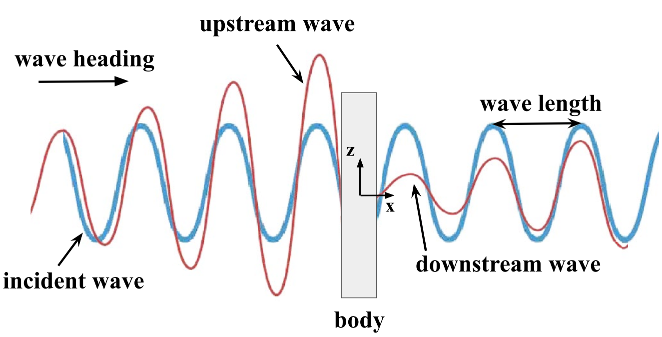

Fig. 7. Representation of the incident, upstream, and downstream wave elevation with respect to the WEC device.

$$S(\omega) = H_s^2 \frac{5}{16} \frac{\omega_p^4}{\omega^5} e^{-\frac{5}{4}\left(\frac{\omega_p}{\omega}\right)^4} \tag{8}$$

where ω_p is the peak wave frequency [rad/s]. This spectrum is shown in the Appendix for reference. For each frequency, the significant wave height was multiplied by the corresponding transmission (or reflection) coefficient to represent the reduced (or increased) wave height due to a WEC device. This can be represented as

$$\hat{S}_t(\omega) = S(\omega)K_t^2(\omega) \tag{9}$$

where $\hat{S}(\omega)$ signifies the spectrum adjusted by either the transmission (*t*) or reflection (*r*) coefficients. The coefficient is squared because it is a multiplier to significant wave height (H_s), which is squared in the spectrum equation. The expected value for the altered significant wave height can be found using the zeroth moment (m_0) of the spectrum[47]:

$$\hat{H}_s = 4\sqrt{m_0} \tag{10}$$

where[48]

$$m_0 = \int_{-\infty}^{\infty} \hat{S}(\omega)d\omega \tag{11}$$

Finally, the expected wave height reduction (or reflection) in irregular waves can be found by

$$K_{irr} = \frac{\hat{H}_s}{H_s} \tag{12}$$

This form of the coefficients was used in the far-field model. Though these coefficients are computed by the numerical model, their is propagated measurement uncertainty from the *RAO* measurement in Eq. 5. This results in ±0.00216 uncertainty in the coefficient computation. This corresponds to less than 1% uncertainty due to experimental measurements in the K_t prediction and between 2 and 10% uncertainty for K_r. Details on the uncertainty analysis are provided in the Uncertainty section.

Far-field model

Solving for the hydrodynamic properties of the devices helps describe the energy propagation through the system, but this method does not account for factors such as varying bathymetry, wind inputs, and other physical parameters of the ocean environment. Additionally, the BEM solver is only computationally efficient at resolving the free surface on the order of a few hundred meters[49]. WEC farms and offshore wind farms may be as far as several kilometers apart, requiring a different approach for determining the far-field effects on the wave environment. Therefore, a spectral approach is taken to model the far-field wave height. The spectral approach relies on statistical properties of the sea surface and linear wave theory. This modeling is done through the open-source software Simulating WAves Nearshore (SWAN)[50].

In SWAN, the devices are modeled as "obstacles" with a specified position, length, and transmission and reflection coefficient. The transmission ($K_{t,irr}$) and reflection ($K_{r,irr}$) coefficients defined above act as multipliers to the energy density at the grid lines that intersect with an obstacle line. Specific details on the numerical implementation of the coefficients can be found in the SWAN documentation[50]. A depiction of how the hydrodynamic and far-field solvers interact is shown in Fig. 5a.

The oceanic conditions selected for this work are based on the South Fork Wind Farm development, located about 19 miles southeast of Block Island, Rhode Island[51], spanning about 24 km2. Bathymetry, significant wave height, and peak period data are used for the far-field wave reduction analysis. Bathymetry data was obtained through the Northeast Ocean data explorer[52] and used to define the sea floor location on the computational grid. Wave conditions were obtained from NOAA Buoy 44097[53], and the corresponding spectra was defined from the fluid domain boundaries. This farm hosts 12 monopile turbines rated at 6–12 MW each[54] with a total farm rated power of 132 MW. The maximum monopile diameters are 10.97 m[55], which is the largest diameter before upgrading to more expensive jacket structures.

Wave-induced fatigue damage

The force the wave exerts on the monopile (F_{wave}) is quantified using the Morison equation[56], shown as

$$F_{wave} = \frac{\pi}{4}d^2 C_M \rho_w \dot{u} + \frac{1}{2}C_D d\rho_w u|u| \tag{13}$$

where ρ_w is the density of sea water, *d* is the monopile diameter, and C_D and C_M are the dimensionless drag and inertial coefficients, respectively. The drag coefficient is set to one and the inertial coefficient is set to two[57]. Methods exist to account for second-order Stokes wave kinematics (extended Morison model) and diffraction effects around the turbine (MacCamy-Fuchs model[58]). Bachynski and Ormberg[59] compared all three models in their predictions of fatigue damage on 6 and 8 m diameter offshore wind monopiles and towers. They found little to no difference between hydrodynamic modeling methods on total fatigue damage, except a few areas on the tower where the MacCamy-Fuchs method predicted less fatigue damage. However, when the ratio between monopile diameter and wavelength is greater than 0.2 ($D/\lambda > 0.2$), diffraction effects become more relevant[60]. In this study, the dominant wave period at South Fork is 11 s, yielding a 189 m wavelength, with monopile diameters around 11 m. This is well below the threshold where diffraction effects are important to include. Therefore, the traditional Morison model is used in this study. It should be noted that the second-order wave kinematics are relevant when modeling ultimate load states of the turbine components, but this is out of scope of the present study.

The bending moment (M_b) is calculated as

$$M_b = LF_{wave} \tag{14}$$

where L is the draft of the monopile. The axial forces are neglected[61], and the sectional stresses are entirely represented by the bending stress

$$\sigma = \frac{yM_b}{I} \tag{15}$$

where *y* is the distance to the centroidal axis and *I* is the monopile moment of inertia about the y-axis (pitch). The monopile wall thickness was chosen to be 0.125 m based on typical monopile design ranges[62,63], and assumed constant along the submerged depth. The stress range ($\Delta\sigma$) is used to find the number of cycles till failure (N_f) using Whöler's equation[64]

$$N_f = \bar{a}\Delta\sigma^{-m}, \tag{16}$$

where $\log(\bar{a})$ is the intercept of the $\log(N)$ axis on the S-N curve and *m* is the material parameter. For this study, values from the DNV-RP-C203[65] where used. A low stress range was assumed along with $m = 5$, giving an experimentally determined $\log \bar{a}$ value of 13.617. Fatigue damage is then calculated using the Palmgren-Miner rule[66]

$$D = \sum_{i=1}^{n} \frac{n_i}{N_{f,i}}, \tag{17}$$

where *n* signifies each load case (loads from wind, loads from wave, loads from different sea states, etc.), n_i is the number of cycles of that load case, and $N_{f,i}$ is the number of cycles to failure at the stress range of that load case. This study only evaluates the fatigue damage due to wave loading over an offshore wind turbine lifetime of 25 years.

This model includes several simplifications. First, the aerodynamic and coupled wind-wave loads are excluded. These parameters are important for determining the total fatigue damage on the offshore wind turbine; however, the wave-induced loads can account for up to 80% of total fatigue damage depending on turbine size and oceanic conditions[40]. Additionally, the total fatigue damage is sensitive to soil stiffness of the sea floor[40], and this is excluded from the presented model. Therefore, results from the wave-induced fatigue model should be interpreted with some caution, as the full picture of wind turbine fatigue is not captured. This study focuses on the hydrodynamic modeling of the WEC farm and provides a simplified wave-induced fatigue model to demonstrate the potential benefits of co-location outside of power production with a highly developed WEC hydrodynamic near- and far-field model.

Levelized cost

For this study, the energy cost estimate does not account for energy produced by or the cost of the WEC farm. The total energy cost of a hybrid energy system is exceedingly complex and out of scope of the present study, and only the wind farm costs and energy are considered. The levelized cost of energy (*LCOE*, [$/MWh]) is a widely used metric to quantify the cost of energy a system produces, levelized across its lifetime. It is defined as

$$LCOE = \frac{CAPEX_{ann} + OPEX}{AEP} \tag{18}$$

where $CAPEX_{ann}$ [$/kWh/yr] represents the capital costs of the expenditure, annualized by the fixed charge rate (FCR). The *OPEX* [$/kWh/yr] represents the yearly operational and maintenance costs to maintain the energy production system. *AEP* [MWh/MW/yr] stands for annual energy production of the entire system. In this report, the numerator is multiplied by 1000 to report the *LCOE* in $/MWh. The National Lab of the Rockies (NLR) released their 2024 Cost of Wind Energy Review, breaking down costs associated with deploying and operating onshore, offshore fixed-bottom, and offshore floating wind turbines[41]. Their industry- and model-informed cost breakdown was used to estimate the *LCOE* of the South Fork wind farm.

The sheltering provided by the WEC farm allows for the potential to reduce the monopile size of the offshore turbine and/or extend the lifetime of the turbine. As is demonstrated by Eq. 15, the bending stress σ is a function both of the hydrodynamic force induced by the incident wave and the monopile's physical dimensions. If the monopile size is kept constant, reducing the force from the incident wave will reduce the wave-induced fatigue damage and potentially extend its lifetime. If the monopile diameter is reduced, reducing the wave height will still reduce the wave-induced fatigue damage, but the stresses on the smaller diameter with decrease the allowable cycles to failure from wave loading. This can potentially decrease the lifetime of the smaller turbine.

To analyze this tradeoff, specific components of the *LCOE* were altered for two cases. In the first case, the monopile diameter is kept constant at South Fork's size (about 11 m), and the lifetime of the turbine is altered based on the reduction in wave-induced fatigue damage and the amount of the turbine lifetime it consumes. For the second case, the cost of the turbine tower, substructure (monopile), and installation costs of the two are reduced linearly with the reduction in monopile size. The lifetime is adjusted accordingly, and the new *LCOE* is computed.

Experimental validation

Experimental validation was conducted using data from a deep water, non-breaking, non-Stokes fluid regime in the O.H. Hinsdale Directional Wave Basin. Experiments were conducted at the 1:50 scale through Froude scaling similarity laws. The PA array setup in the basin is provided in Fig. 8. Experimental measurements were collected using Qualisys motion capture technology, with four cameras positioned above the array, tracking reflective, massless spheres attached to the buoyant elements of the WECs. This positional data was used to determine the *RAO* for each device across the range of experimental sea states. Resistive and ultrasonic wave gauges were placed throughout the basin to record wave elevation throughout testing, which was compared to the wave elevation prediction by the BEM solver and also required to resolve the *RAO*.

To correct the numerical model's prediction of the hydrodynamic response of the WEC systems, an empirical damping coefficient was introduced for each device in the array. This is an additional damping term, included in Eq. 1 into the total damping term (B_{tot}). We compared the *RAO* predicted by the BEM solver and the *RAO* resolved from experimentation, and the difference between the two was accounted for with this additional damping term. The other hydrodynamic coefficients and wave excitation forces were predicted by the BEM solver. The empirical damping is a model-form correction to account for known limitations of linear potential flow theory. Experiments were conducted to quantify the individual hydrodynamic coefficients and the wave excitation force empirically for comparison to the BEM model. This individual coefficient validation is still underway and will be presented in a separate, so the model-form empirical damping term is used to calibrate the BEM model here.

The results of this empirical fit are shown in Fig. 9aand 9b. Most fits were achieved with 1 st, 2nd, or 3rd order polynomials with R^2 values greater than 0.9800. The Qualisys measurement uncertainty of the *RAOs*, which was used to obtain the empirical fits, resulted in less than 1% error propagation to the derived damping term. Future work includes validation of individual hydrodynamic coefficients before fitting an empirical viscous damping term.

The free surface directly around the devices (near-field) was compared to the BEM model prediction using resistive wave gauges. The root-mean-squared (RMS) amplitude from the wave elevation time-series data was compared to the BEM model free surface elevation computation. The results of this comparison are shown in Fig. 9cthrough 9ffor the scaled wave frequency of 4.52 rad/s. Only one frequency is shown for brevity, but results are discussed for frequencies between 4.52 to 6.28 rad/s, and their figures are shown in the Appendix. At full ocean-scale, this corresponds to wave periods between 7.07 and 9.83 s (0.889 and 0.639 rad/s). At the faster wave frequency, we observe slightly more error overall. This can potentially be attributed to the BEM assumption of small device characteristic dimension with respect to incident wavelength. Error is greatly improved at the slower wave period, similar to the dominant wave period analyzed in this study. However, we do observe over-estimation of the reflected wave height due to the OSWEC array. In terms of wave sheltering, the downstream wave height prediction is more relevant, as it dictates energy propagation towards the offshore wind turbines (or whatever structure is being sheltered). Therefore, we deem the downstream average error of 3.83% for the

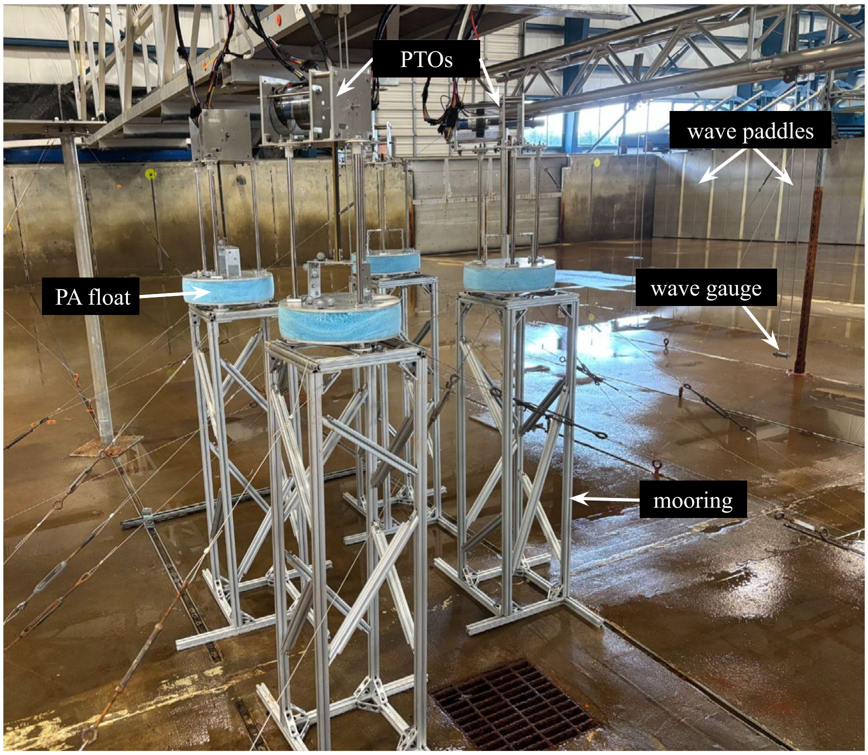

Fig. 8. Four-body PA array setup in the O.H. Hinsdale Directional Wave Basin.

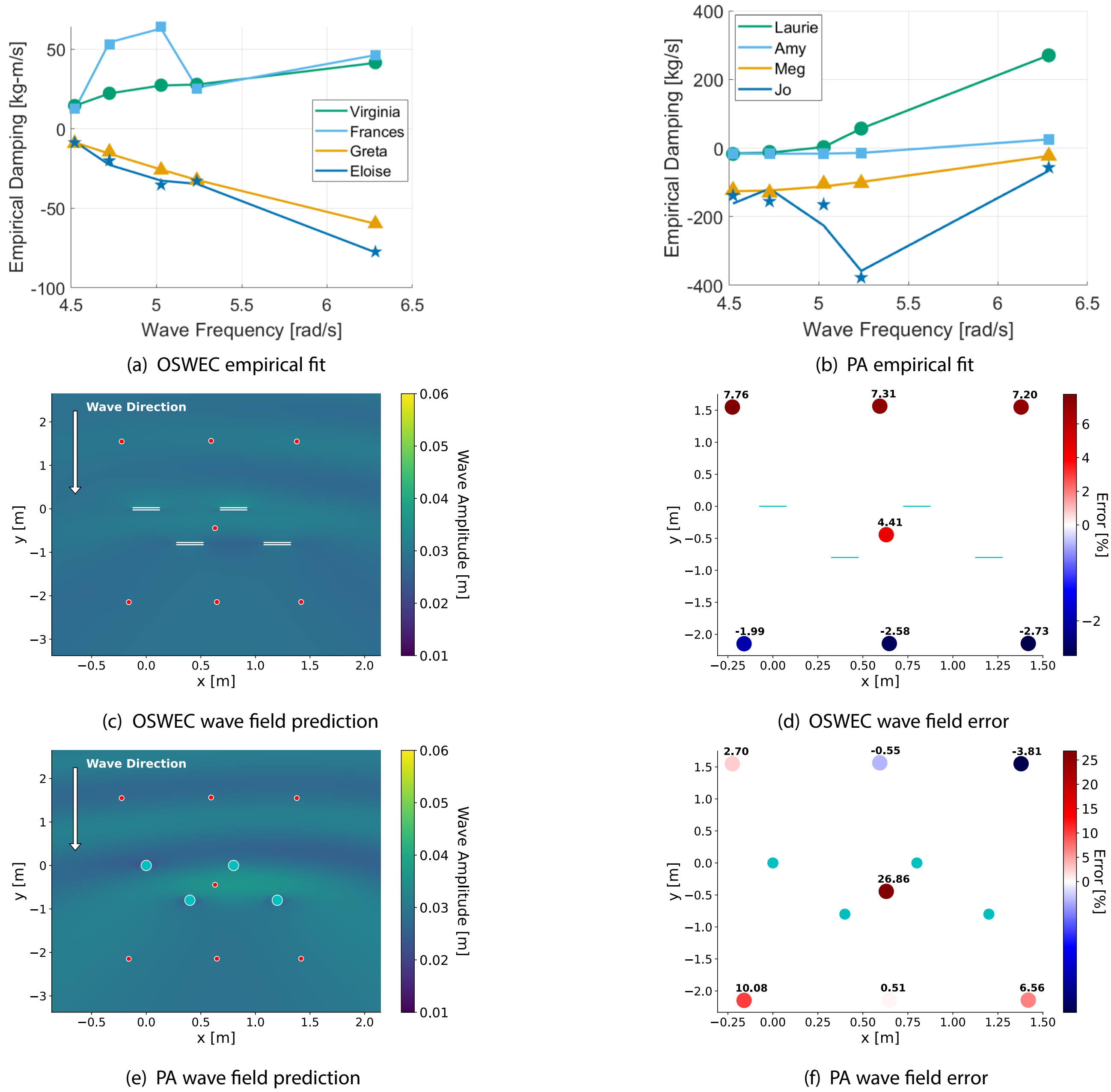

Fig. 9. (**a**) and (**b**) show curve fits for empirically derived damping terms for each device in the (**a**) OSWEC array and (**b**) PA WEC array. Solid lines indicate the curve fit while markers indicate the empirically derived coefficients. The curve fits have R^2 value greater than 0.9800, and the empirical data used to obtain the fits resulted in less than 1% error propagation to the derived damping term. (**c**) and (**e**) show the wave amplitude computed by the BEM solver due to the presence of the WEC array (shown by light blue lines for OSWECs and circles for PAs). The red circles indicate locations of resistive wave gauges in the physical basin. (**d**) and (**f**) show the percent error at each probe. Values greater than zero indicate an over-prediction in wave amplitude, while values less than zero indicate an under-prediction.

OSWECs and 5.72% for the PAs in the $\omega = 4.52$ rad/s case to be acceptable. No tuning or correction was made directly for the free surface elevation prediction, and all free surface computations used in the results are forward predictions based on the calibrated device *RAOs*.

Uncertainty

The bias/random uncertainty of the experimental measurements was determined using a bootstrap analysis[67]. This analysis produces shorter time series chunks of the original full-length time series. These smaller chunks of the data are then statistically analyzed individually and ensembled to determine the distribution of different statistical measurements. For example, the mean of each smaller chunk of the larger time series would be computed, and the distribution of all of the means is the output. Therefore, we report the statistically most probable mean value of the entire time series within 95% confidence interval bounds of the distribution of smaller time-series means.

For computed values, the measurement uncertainty from each variable included in the computation propagates to the final output. The method developed by Kline and McClintock[68] was followed to represent this uncertainty propagation. In this method, the total result uncertainty is defined as *R*, where *R* is some function of the measured variables. The contribution of each measured variable's uncertainty (δR_{x_i}) to the result uncertainty (δR) is defined as

$$\delta R_{x_i} = \frac{\partial R}{\partial x_i} \delta x_i \tag{19}$$

where x_i denotes the measured variables and δx_i is the uncertainty in their measurement, obtained through the bootstrap analysis of the measured time series. The total result uncertainty is then determined by the root-sum-squared (RSS) of the contributions of each measured variable's uncertainty, shown as

$$\delta R = \sqrt{\sum_i (\delta R_{x_i})^2} \tag{20}$$

The uncertainty reported in Fig. 6 was computed using the bootstrap analysis. This is due to device motion and wave elevation being experimental measurements. The experimentally measured *RAO* was used to compute the empirical damping coefficients, and the uncertainty propagation analysis was conducted for this damping term and the K_t and K_r coefficients.

Data availability

The open-source code can be found at the SEA Lab GitHub Repository https://github.com/symbiotic-engineering/transmission-reflection/releases/tag/hybrid_wind_wave The open-source experimental dataset can be accessed at the Marine and Hydrokinetic Data Repository https://mhkdr.openei.org/submissions/637.

Received: 12 December 2025; Accepted: 20 May 2026
Published online: 12 June 2026

References

1. Díaz, H. & Guedes Soares, C. Review of the current status, technology and future trends of offshore wind farms. *Ocean Eng.* **209**, 107381. https://doi.org/10.1016/j.oceaneng.2020.107381 (2020).
2. GWEC's Global Offshore Wind Report (2025).
3. Shao, H., Henriques, R., Morais, H. & Tedeschi, E. Power quality monitoring in electric grid integrating offshore wind energy: A review. *Renewable and Sustainable Energy Reviews* **191**, 114094. https://doi.org/10.1016/j.rser.2023.114094 (2024).
4. Ren, G., Liu, J., Wan, J., Guo, Y. & Yu, D. Overview of wind power intermittency: Impacts, measurements, and mitigation solutions. *Appl. Energy* **204**, 47–65. https://doi.org/10.1016/j.apenergy.2017.06.098 (2017).
5. Veigas, M. & Iglesias, G. Potentials of a hybrid offshore farm for the island of Fuerteventura. *Energy Convers. Manag.* **86**, 300–308. https://doi.org/10.1016/j.enconman.2014.05.032 (2014).
6. Del Pozo Gonzalez, H., Bianchi, F. D., Dominguez-Garcia, J. L. & Gomis-Bellmunt, O. Co-located wind-wave farms: Optimal control and grid integration. *Energy* **272**, 127176. https://doi.org/10.1016/j.energy.2023.127176 (2023).
7. Pérez-Collazo, C., Greaves, D. & Iglesias, G. A review of combined wave and offshore wind energy. *Renew. Sustain. Energy Rev.* **42**, 141–153. https://doi.org/10.1016/j.rser.2014.09.032 (2015).
8. Michailides, C., Gao, Z. & Moan, T. Experimental study of the functionality of a semisubmersible wind turbine combined with flap-type wave energy converters. *Renewable Energy* **93**, 675–690. https://doi.org/10.1016/j.renene.2016.03.024 (2016).
9. Jariwala, A. M., Dash, S. K., Sahu, U. K. & Chudjuarjeen, S. Design and dynamic emulation of hybrid solar-wind-wave energy converter (swwec) for efficient power generation. *Sci Rep* https://doi.org/10.1038/s41598-024-72827-9 (2024).
10. Zhao, X., Huang, G., Li, Y., Lu, C., Tian, C., Song, T. & Pang, B. Offshore wave and wind energy development in the southern hemisphere will remain optimal between 20°e and 180°e by 2100. *Commun Earth Environ* https://doi.org/10.1038/s43247-025-02437-4 (2025).
11. Sebastian, B., Karmakar, D. & Rao, M. Dynamic behaviour and power performance of a septon semisubmersible floating wind turbine integrated with wave energy converters. *Sci Rep.* https://doi.org/10.1038/s41598-025-25012-5 (2025).
12. Kluger, J. M., Haji, M. N. & Slocum, A. H. The power balancing benefits of wave energy converters in offshore wind-wave farms with energy storage. *Applied Energy* **331**, 120389. https://doi.org/10.1016/j.apenergy.2022.120389 (2023).
13. Astariz, S., Perez-Collazo, C., Abanades, J. & Iglesias, G. Co-located wind-wave farm synergies (operation i& maintenance): A case study. *Energy Convers. Manag.* **91**, 63–75. https://doi.org/10.1016/j.enconman.2014.11.060 (2015).
14. Fernandez, H. et al. The new wave energy converter Wavecat: Concept and laboratory tests. *Mar. Struct.* **29**, 58–70. https://doi.org/10.1016/j.marstruc.2012.10.002 (2012).
15. Sun, C. & Jahangiri, V. Fatigue damage mitigation of offshore wind turbines under real wind and wave conditions. *Eng. Struct.* **178**, 472–483. https://doi.org/10.1016/j.engstruct.2018.10.053 (2019).
16. Saenz-Aguirre, A., Ulazia, A., Ibarra-Berastegi, G. & Saenz, J. Floating wind turbine energy and fatigue loads estimation according to climate period scaled wind and waves. *Energy Conversion and Management* **271**, 116303. https://doi.org/10.1016/j.enconman.2022.116303 (2022).
17. Achmus, M., Kuo, Y.-S. & Abdel-Rahman, K. Behavior of monopile foundations under cyclic lateral load. *Comput. Geotech.* **36**, 725–735. https://doi.org/10.1016/j.compgeo.2008.12.003 (2009).
18. Häfele, J., Hübler, C., Gebhardt, C. G. & Rolfes, R. A comprehensive fatigue load set reduction study for offshore wind turbines with jacket substructures. *Renew. Energy* **118**, 99–112. https://doi.org/10.1016/j.renene.2017.10.097 (2018).
19. Pustina, L., Lugni, C., Bernardini, G., Serafini, J. & Gennaretti, M. Control of power generated by a floating offshore wind turbine perturbed by sea waves. *Renew. Sustain. Energy Rev.* **132**, 109984. https://doi.org/10.1016/j.rser.2020.109984 (2020).
20. Christiansen, S., Bak, T. & Knudsen, T. Damping wind and wave loads on a floating wind turbine. *Energies* **6**, 4097–4116. https://doi.org/10.3390/en6084097 (2013).

21. Flanagan, T., Wengrove, M. & Robertson, B. Coupled wave energy converter and nearshore wave propagation models for coastal impact assessments. *J. Mar. Sci. Eng.* **10**, 370. https://doi.org/10.3390/jmse10030370 (2022).
22. Chang, G., Ruehl, K., Jones, C., Roberts, J. & Chartrand, C. Numerical modeling of the effects of wave energy converter characteristics on nearshore wave conditions. *Renew. Energy* **89**, 636–648. https://doi.org/10.1016/j.renene.2015.12.048 (2016).
23. Venugopal, V., Nemalidinne, R. & Vögler, A. Numerical modelling of wave energy resources and assessment of wave energy extraction by large scale wave farms. *Ocean I& Coastal Management* **147**, 37–48, https://doi.org/10.1016/j.ocecoaman.2017.03.012 (2017). Tools for managing the development of the wave and tidal energy resource (TeraWatt).
24. Contardo, S. et al. In situ observations and simulations of coastal wave field transformation by wave energy converters. *Coast. Eng.* **140**, 175–188. https://doi.org/10.1016/j.coastaleng.2018.07.008 (2018).
25. Atan, R., Finnegan, W., Nash, S. & Goggins, J. The effect of arrays of wave energy converters on the nearshore wave climate. *Ocean Engineering* **172**, 373–384. https://doi.org/10.1016/j.oceaneng.2018.11.043 (2019).
26. Silva, D., Rusu, E. & Guedes Soares, C. The effect of a wave energy farm protecting an aquaculture installation. *Energies* **11**, 2109. https://doi.org/10.3390/en11082109 (2018) (Submission received: 7 July 2018 / Revised: 5 August 2018 / Accepted: 6 August 2018 / Published: 13 August 2018.).
27. Carballo, R. & Iglesias, G. Wave farm impact based on realistic wave-WEC interaction. *Energy* **51**, 216–229. https://doi.org/10.1016/j.energy.2012.12.040 (2013).
28. Babarit, A. On the park effect in arrays of oscillating wave energy converters. *Renew. Energy* **58**, 68–78. https://doi.org/10.1016/j.renene.2013.03.008 (2013).
29. Balitsky, P. A numerical investigation of the array effects of wave energy converters with a realistic power take-off system utilizing a coupled model suite. Ph.D. thesis, Ghent University. (2019).
30. Zou, S. et al. Wave energy converter arrays: A methodology to assess performance considering the disturbed wave field. *Renew. Energy* **229**, 120719. https://doi.org/10.1016/j.renene.2024.120719 (2024).
31. Clark, C. E. & Paredes, G. M. Effects of co-located floating wind-wave systems on fatigue damage of floating offshore wind turbine mooring cables. In *Proceedings of the ASME 2018 1st International Offshore Wind Technical Conference*, International Conference on Offshore Mechanics and Arctic Engineering, V001T01A024, https://doi.org/10.1115/IOWTC2018-1077 (2018).
32. Clark, C. E., Velarde, J. & Sønderkær Nielsen, J. Fatigue load reductions in offshore wind turbine monopile foundations in co-located wind-wave arrays. In *Proceedings of the ASME 2018 1st International Offshore Wind Technical Conference*, International Conference on Offshore Mechanics and Arctic Engineering, V001T01A037, https://doi.org/10.1115/IOWTC2018-1024 (2018).
33. Seelig, W. N. Two-dimensional tests of wave transmission and reflection characteristics of laboratory breakwaters. Tech. Rep. NO. 80-1, Q TECHNICAL REPORT (1980).
34. Bao, L. et al. Research on wave and energy reduction performance of floating breakwater based on s-shaped runner. *Energies* **15**, 5148. https://doi.org/10.3390/en15145148 (2022).
35. Energy, C. C. *Ceto harnessing the ocean's power*.
36. CorPower. Wave energy, finally unlocked.
37. Impulse, S. & Waveroller.
38. Neary, V., LaBonte, A., Rieks, J. & Copping, A. Reference model project: Point designs, methodologies, and tools to support open-source mhk r&d. 3rd Annual Marine Energy Technology Symposium (METS) (METS, 2015).
39. Vitale, O. et al. Design, build, and analysis of small-scale wave energy converter prototypes. *J. Mech. Des.* **148**, 091701. https://doi.org/10.1115/1.4070757 (2026).
40. Sørum, S. H., Krokstad, J. R. & Amdahl, J. Wind-wave directional effects on fatigue of bottom-fixed offshore wind turbine. *Journal of Physics: Conference Series* **1356**, 012011. https://doi.org/10.1088/1742-6596/1356/1/012011 (2019).
41. Tyler Stehly, P. D. & Hernando, D. M. Cost of wind energy review: 2024 edition (2024).
42. Falnes, J. & Kurniawan, A. *Ocean Waves and Oscillating Systems: Linear Interactions Including Wave-Energy Extraction*. Cambridge Ocean Technology Series (Cambridge University Press, 2020), 2 edn.
43. Ancellin, M. & Dias, F. Capytaine: A Python-based linear potential flow solver. *J. Open Source Softw.* **4**, 1341. https://doi.org/10.21105/joss.01341 (2019).
44. K. Khanal, N. D., O. Vitale. Multi-objective multidisciplinary optimization of wave energy converter array configurations and controls. In *Proceedings of DOE WPTO University Marine Energy Research Community (UMERC) Conference.* (October 4–6, 2023).
45. Comparison of existing methods for the calculation of the infinite water depth free-surface green function for the wave-structure interaction problem. *Applied Ocean Research* **81**, 150–163. https://doi.org/10.1016/j.apor.2018.10.007 (2018).
46. Hwang, S. & Lee, J. L. Extraction of wave height-period joint probability distribution from empirical frequency spectrum. *Ocean Engineering* **308**, 118222. https://doi.org/10.1016/j.oceaneng.2024.118222 (2024).
47. Boccotti, P. Chapter 3 - random wind-generated waves: Basic concepts. In *Wave Mechanics and Wave Loads on Marine Structures* (ed. Boccotti, P.) 43–61 (Butterworth-Heinemann, 2015). https://doi.org/10.1016/B978-0-12-800343-5.00003-2.
48. Gherbi, A. & Belgasmia, M. Chapter 21 - stochastic analysis basics and application of statistical linearization technique on a controlled system with nonlinear viscous dampers. In *Handbook of Probabilistic Models* (eds Samui, P. et al.) 505–525 (Butterworth-Heinemann, 2020). https://doi.org/10.1016/B978-0-12-816514-0.00021-7.
49. Ancellin, M., Marchand, P. & Dias, F. Towards high-performance linear potential flow bem solver with low-rank compressions. *Energies* https://doi.org/10.3390/en17020372 (2024).
50. Delft University of Technology. Simulating waves nearshore v40.45 (2024). Accessed: 2024-05-21.
51. of Ocean Energy Management, B. South fork boem renewable energy lease area ocs-a 0517, (2022).
52. Northeast Ocean Data. Northeast ocean data explorer. https://www.northeastoceandata.org/data-explorer/. Accessed: 22-May-2024.
53. National Data Buoy Center. Station 44097 - northeastern gulf of maine. https://www.ndbc.noaa.gov/station_page.php?station=44097. Accessed: 22-May-2024.
54. Tethys. South fork wind. https://tethys.pnnl.gov/wind-project-sites/south-fork-wind. Accessed: 22-May-2024.
55. Denes, S., Weirathmueller, M. & Zeddies, D. Foundation installation at south fork wind farm: Animal exposure modelling. Tech. Rep. P001383-002, Document 01726, Version 2.0, JASCO Applied Sciences (USA) Inc., Silver Spring, MD, USA (2020). Submitted to: Jeff Nield, Jacobs Engineering Group Inc., Agreement number: 10381-7-120889.
56. Morison, J., Johnson, J. W. & Schaaf, S. A. The force exerted by surface waves on piles. *J. Pet. Technol.* **2**, 149–154 (1950).
57. Agerschou, H. A. & Edens, J. J. Fifth and first order wave-force coefficients for cylindrical piles. In *Proceedings of the Conference on Wave Forces*, chap. 10 (Frederic R. Harris, Inc. and Van Houten, SchHartz and Nurphy, New York, N. Y., 1965).
58. MacCamy RC, F. R. Wave forces on piles: a diffraction theory (1954).
59. Bachynski, E. & Ormberg, H. Hydrodynamics modeling of large-diameter bottom-fixed offshore wind turbines. In *Proceedings of the ASME 34th International Conference on Ocean, Offshore and Arctic Engineering* (2015).
60. Sarpkaya, T. S., Isaacson, M. S. & Wehausen, J. V. Mechanics of wave forces on offshore structures (1981).
61. Velarde, J. & Bachynski, E. E. Design and fatigue analysis of monopile foundations to support the DTU 10 MW offshore wind turbine. *Energy Procedia* **137**, 3–13. https://doi.org/10.1016/j.egypro.2017.10.330 (2017).
62. Mendoza, A. S. E., Griffith, D. T., Qin, C., Loth, E. & Johnson, N. Rapid approach for structural design of the tower and monopile for a series of 25 mw offshore turbines. *Journal of Physics: Conference Series* **2265**, 032030. https://doi.org/10.1088/1742-6596/2265/3/032030 (2022).

63. Limited, B. F. T. Fatigue design review of offshore wind turbine generator structures: Final report. Technical Report, United States Department of the Interior, Bureau of Safety and Environmental Enforcement, Acquisition Operations Branch, MS2101, 381 Elden Street, Herndon, VA 20170. Submitted to Altan Aydin. BMT Contact: Dale Braun, PEng. Tel: 613-592-2830, Ext. 333. Fax: 613-592-4950.
64. Yeter, B., Garbatov, Y. & Guedes Soares, C. Fatigue damage assessment of fixed offshore wind turbine tripod support structures. *Eng. Struct.* **101**, 518–528. https://doi.org/10.1016/j.engstruct.2015.07.038 (2015).
65. Det Norske Veritas AS. Fatigue Design of Offshore Steel Structures: Recommended Practice. Det Norske Veritas AS (2010) (DNV-RP-C203).
66. Miner, M. A. Cumulative Damage in Fatigue. *Journal of Applied Mechanics* **12**, A159–A164. https://doi.org/10.1115/1.4009458 (1945).
67. Efron, B. Bootstrap methods: Another look at the jackknife. *Ann. Statist.* https://doi.org/10.1214/aos/1176344552 (1979).
68. Kline, S. J. Describing uncertainties in single-sample experiments. *Mechanical Engineering* **75**, 3–8 (1953).

Acknowledgements
We would like thank Dr. Alaa Ahmed and Yashaswini Mandalam for their assistance in the experimental campaign and data processing.

Author contributions
O.V. conceived the modeling techniques, executed model implementation, conducted experimental campaign, and developed data analysis techniques. O.V. and M.H. developed the numerical model, developed the experimental campaign, and analyzed results. O.V. and M.H. jointly acquired funding from the Cornell Atkinson Center for Sustainability and from the U.S. Department of Energy. M.H. acquired funding from the New York Sea Grant. All authors reviewed the manuscript.

Funding
This work was funded in part by the Sea Grant Regional Research Project No.: R/ATD-18-NESG, the Cornell Atkinson Center for Sustainability through the 2023 Summer Mentored Research Program and the 2025 FAST Grant, and the U.S. Department of Energy through Testing and Expertise in Marine Energy (TEAMER) RFTS 12.

Declarations

Competing interests
The authors declare no competing interests.

Additional information
Supplementary Information The online version contains supplementary material available at https://doi.org/10.1038/s41598-026-54843-z.

Correspondence and requests for materials should be addressed to O.V.

Reprints and permissions information is available at www.nature.com/reprints.

Publisher's note Springer Nature remains neutral with regard to jurisdictional claims in published maps and institutional affiliations.